Tectonics

RESEARCH ARTICLE
10.1029/2020TC006572

Key Points:

- Continuous fluid supply causes shear zone widening
- Shear zones widen during strain accumulation

Supporting Information:

- Supporting Information S1
- Figure S1
- Figure S2
- Figure S3
- Figure S4
- Figure S5
- Figure S6
- Data Set S1

Correspondence to:

L. Kaatz and T. John,
lisa.kaatz@fu-berlin.de;
timm.john@fu-berlin.de

Citation:

Kaatz, L., Zertani, S., Moulas, E., John, T., Labrousse, L., Schmalholz, S. M., & Andersen, T. B. (2021). Widening of hydrous shear zones during incipient eclogitization of metastable dry and rigid lower crust—Holsnøy, western Norway. *Tectonics*, *40*, e2020TC006572. https://doi.org/10.1029/2020TC006572

Received 14 OCT 2020
Accepted 12 JAN 2021

Widening of Hydrous Shear Zones During Incipient Eclogitization of Metastable Dry and Rigid Lower Crust—Holsnøy, Western Norway

Lisa Kaatz[1], Sascha Zertani[1], Evangelos Moulas[2], Timm John[1], Loïc Labrousse[3], Stefan M. Schmalholz[4], and Torgeir B. Andersen[5]

[1]Institute of Geological Sciences, Freie Universität Berlin, Berlin, Germany, [2]Institute of Geosciences, Johannes Gutenberg-Universität Mainz, Mainz, Germany, [3]Institut des Sciences de la Terre Paris, Sorbonne Université, UMR 7193, Paris, France, [4]Institute of Earth Sciences, University of Lausanne, Géopolis, Lausanne, Switzerland, [5]Department of Geosciences, Centre of Earth Evolution and Dynamics (CEED), University of Oslo, Oslo, Norway

Abstract The partially eclogitized crustal rocks on Holsnøy in the Bergen Arcs, Norway, indicate that eclogitization is caused by the interplay of brittle and ductile deformation promoted by fluid infiltration and fluid-rock interaction. Eclogitization generated an interconnected network of millimeter-to-kilometer-wide hydrous eclogite-facies shear zones, which presumably caused transient weakening of the mechanically strong lower crust. To decipher the development of those networks, we combine detailed lithological and structural mapping of two key outcrops with numerical modeling. Both outcrops are largely composed of preserved granulite with minor eclogite-facies shear zones, thus representing the beginning phases of eclogitization and ductile deformation. We suggest that deformation promoted fluid-rock interaction and eclogitization, which gradually consumed the granulite until fluid-induced reactions were no longer significant. The shear zones widen during progressive deformation. To identify the key parameters that impact shear zone widening, we generated scale-independent numerical models, which focus on different processes affecting the shear zone evolution: (i) rotation of the shear zones caused by finite deformation, (ii) mechanical weakening due to a limited amount of available fluid, and (iii) weakening and further hydration of the shear zones as a result of continuous and unlimited fluid supply.

A continuous diffusion-type fluid infiltration, with an effective diffusion coefficient around $D = 10^{-16}\,\frac{\mathrm{m}^2}{\mathrm{s}}$, coupled with deformation is prone to develop structures similar to the ones mapped in field. Our results suggest that the shear zones formed under a continuous fluid supply, causing shear zone widening, rather than localization, during progressive deformation.

1. Introduction

Seismic imaging of subduction and continental collision zones suggests that slabs often comprise strong and dry lower crustal rocks, which progressively transform into denser eclogites (Nábělek et al., 2009; Rondenay et al., 2008; Schneider et al., 2013; Yuan et al., 2000). While eclogitization can be kinetically delayed (e.g., Austrheim, 1987; John & Schenk, 2003; Labrousse et al., 2010) it is typically promoted by the interplay of brittle and ductile deformation, which facilitates fluid infiltration (e.g., Austrheim, 1987; Jamtveit et al., 2019; John & Schenk, 2003). In fact, only limited amounts of fluid are required to overcome the metastable state and trigger mineral reactions (e.g., Austrheim, 1987; Menegon et al., 2017). Metamorphic hydration from an external fluid results in temporary weakening and enhances the conversion of originally dry crustal rocks (e.g., Chen et al., 2006; Klemd et al., 2011). Consequently, metamorphic reactions initiated by fluid infiltration influence the rock strength (e.g., Gerald & Stünitz, 1993). Furthermore, the newly formed phases often have significantly smaller grain sizes compared to their precursors (e.g., Putnis & John, 2010), which enhances weakening if a grain size-sensitive deformation mechanism is activated (e.g., Hawemann et al., 2019; Hier-Majumder, 2005; Karato & Jung, 2003). In addition, weaker zones are likely to interconnect and hence, channelize the eclogitization process (e.g., Raimbourg et al., 2007). Consequently, when hydrous, fine-grained eclogites, which are connected in a network, develop in a strong continental crust, they will cause a dramatic decrease of the bulk crustal strength. Previous investigations combined with experimental results led to the conclusion that rocks, which develop during fluid-assisted eclogitization,

are ~1 order of magnitude weaker than their metastable precursors, such as granulites (e.g., Labrousse et al., 2010; Terry & Heidelbach, 2006). The resulting spatial strength variations likely also cause spatial pressure variations during deformation (e.g., Jamtveit et al., 2018b; Mancktelow, 2008; Moulas et al., 2019).

Contrary to the common assumption that hydrous and weak shear zones localize and thin, field observations on the island of Holsnøy suggest that the fluid-induced eclogite-facies shear zones (that crosscut dry granulites) widen during progressive deformation and strain accumulation (e.g., Austrheim & Griffin, 1985; Boundy et al., 1992; Jolivet et al., 2005). Shear zone widening, however, would imply strain hardening rather than strain softening (e.g., Jessell & Lister, 1991). Recently, Fossen & Cavalcante (2017) compared published structural field data from different locations and developed a generalized classification of four ideal shear zone types characterized by the evolution of their thickness and strain distribution through time. One main result of this comparison is a generally increasing shear zone width during strain accumulation. Potential reasons for shear zone thickening are various, for example, metamorphic growth of stronger minerals inside the shear zone center, changes in the deformation mechanism, geometric causes like competent objects within the shear zones, folds, host rock softening (Fossen & Cavalcante, 2017) or thermal conduction for ductile shear zones controlled by thermal softening (e.g., Kiss et al., 2019). In fact, only a few field-based studies explicitly discuss the evolution of shear zone thickness during strain accumulation and most of them do not show a positive displacement-thickness relationship as described in Fossen & Cavalcante (2017). For instance, Pennacchioni and Mancktelow (2018) demonstrated that the structural evolution of ductile amphibolite-facies shear zones of the Neves area (Eastern Alps, Italy) is predetermined by their precursor structures, for example, fractures and dykes. Despite the fluid-rich environment these ductile shear zones do not widen with increasing strain. Another example is given by the study of Hawemann et al. (2019) reporting that the shear zones of the exhumed dry lower crustal rocks of the Musgrave Range in central Australia are limited in thickness by their precursor geometry (e.g., fractures). Also, in the Lofoten, viscously reactivated pseudotachylytes do not show any widening, due to limited fluid infiltration (Menegon et al., 2017).

Here, we assess the effect of fluid availability during viscous deformation on shear zone widening. We conducted a first-order quantitative study combining detailed structural and lithological mapping (centimeter to meter scale) of two representative outcrops with petrological analysis of the corresponding lithologies. Based on this study, we perform two-dimensional (2-D) numerical simulations to deduce the factors controlling shear zone widening. Viscous deformation and fluid infiltration are key processes that control the style of deformation during shear zone evolution. Therefore, we investigate how these processes influence the geometrical evolution of hydrous shear zones during eclogitization with respect to the regional far-field stress. Particularly, in our numerical model, we describe fluid infiltration with a simple diffusion-type model and the rheological weakening effects of eclogitization with a viscosity that depends on the diffusing fluid. We use the simulations to determine the effective fluid diffusivity for which the geometry and widening of the modeled viscous shear zones agree with the natural shear zones. Furthermore, we discuss strain partitioning, the resulting pressure variations, and changes in rheology.

2. Geological Setting

The structure of western Norway is largely controlled by the Scandian phase of the Caledonian orogeny (e.g., Corfu et al., 2014; Roberts, 2003). During the collision of Baltica and Laurentia, parts of Baltica and its hyperextended pre-Caledonian continental margin was subducted beneath Laurentia (Figure 1a; Andersen et al., 1991, 2012; Jakob et al., 2017). Subsequently, large nappes including continental crust of the Jotun microcontinent, which was located outboard of the hyperextended domain with exhumed mantle (heM in Figure 1a), were thrust SE-wards onto Baltica forming the Bergen Arc System (e.g., Fossen & Dunlap, 1998; Gee & Sturt, 1985; Roberts, 2003). These microcontinental slivers included the Lindås, Jotun, and Dalsfjord nappes (e.g., Jakob et al., 2017, 2019). The Lindås-Dalsfjord-Jotun nappe complexes are structurally overlain by ophiolite-island-arc complexes and related oceanic rocks from the Iapetus Ocean (orIO in Figure 1a). The crystalline basement nappes mostly consist of Middle Proterozoic orthogneisses including anorthositic granulites, mangerites, jotunites, metagabbros, and various granitoid gneisses, which, experienced Caledonian eclogite-to-amphibolite-facies overprint between ~430 ± 3.5 Ma and 423 ± 1.0 Ma (e.g., Austrheim, 1987; Austrheim & Griffin, 1985; Glodny et al., 2008; Jamtveit et al., 2018b). Different studies in the Lindås nappe imply various eclogite-facies peak pressure and temperature (P-T)-conditions mostly

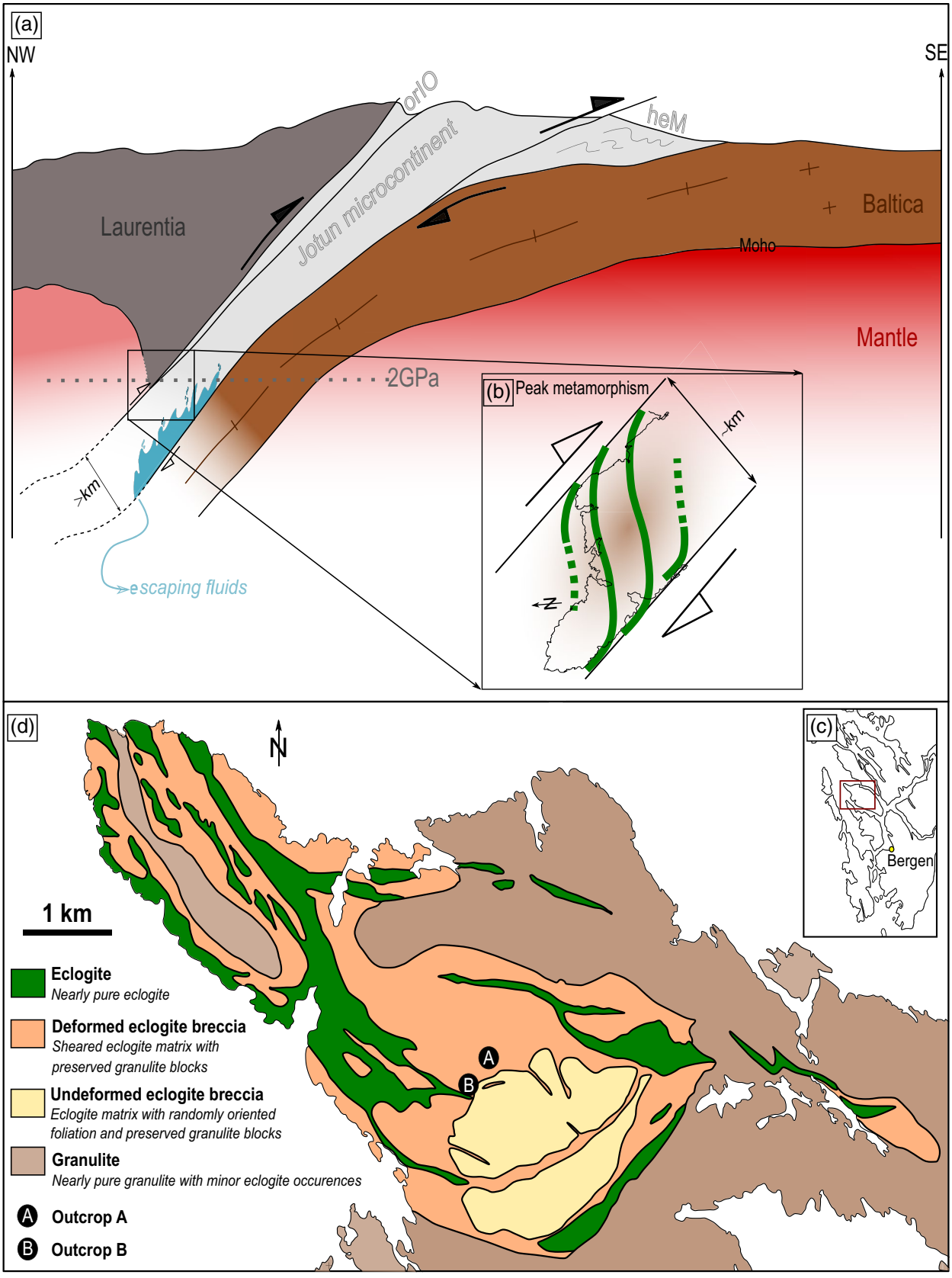
(a)
NW
SE
orIO
heM
Laurentia
Jotun microcontinent
Baltica
Moho
Mantle
2GPa
~km
escaping fluids
(b) Peak metamorphism
~km
N
(c)
Bergen
(d)
N
1 km
Eclogite
Nearly pure eclogite
Deformed eclogite breccia
Sheared eclogite matrix with preserved granulite blocks
Undeformed eclogite breccia
Eclogite matrix with randomly oriented foliation and preserved granulite blocks
Granulite
Nearly pure granulite with minor eclogite occurences
A Outcrop A
B Outcrop B

accepting temperatures of ~700°C and pressures of ~2 GPa (e.g., Bhowany et al., 2018; Jamtveit et al., 1990; Kühn et al., 2002), whereas the Dalsfjord nappe and its metasedimentary cover experienced an earlier lower-grade HP-LT metamorphism at ~450 Ma (Andersen et al., 1998; Eide et al., 1999).

The studied outcrops on Holsnøy represent a part of the lower crust of the Jotun microcontinent, which was deformed during the Caledonian orogeny (Figure 1). On Holsnøy, it has been documented that eclogitization was initiated by brittle deformation which enabled fluid infiltration (Austrheim, 1987; Jamtveit et al., 2018a; Petley-Ragan et al., 2018) into the granulite-facies anorthosites and gabbros. Although the origin of the external fluid is still a matter of debate, a likely fluid source are the sediments of the basin of the transitional crust in the hyperextended domain that had formed inboard of the Jotun-microcontinent prior to the collision (Andersen et al., 2012; Jakob et al., 2019). This hyperextended domain was overthrust by the Lindås-Jotun nappe complex during early stages of the Scandian collision. The escaping fluids might be responsible for triggering the eclogitization process at peak metamorphic conditions (Figure 1a; e.g., Austrheim, 1987, 1998; Glodny et al., 2008). The newly formed eclogite was mechanically weaker than the surrounding granulite and, thus more susceptible to ductile deformation, promoting the formation of eclogite-facies shear zones (e.g., Austrheim, 1987). This process resulted in an extremely heterogenous distribution of the accumulated strain and the effective eclogitization on Holsnøy (Austrheim, 1987; Boundy et al., 1992; Jolivet et al., 2005; Raimbourg et al., 2005; Zertani et al., 2019b). Therefore, previous studies categorize the exposed lithologies with respect to the abundance of eclogite linked with the apparent strain (Figure 1d; e.g., Boundy et al., 1992; Schmid et al., 1998; Zertani et al., 2019b). Typically, four different lithological domains are described (Austrheim, 1987; Austrheim & Griffin, 1985; Boundy et al., 1992; Raimbourg et al., 2005) ranging from almost undeformed and very minor eclogitized regions to highly deformed and pervasively eclogitized zones. These are as follows: (1) unaltered granulites, (2) areas where granulites are cut by narrow eclogite bands originating from fracture-related fluid infiltration, (3) eclogite breccias, where granulite blocks are surrounded by an eclogite matrix, and (4) well-developed eclogite shear zones, up to hundreds of meters wide (high-strain, e.g., Boundy et al., 1992; Raimbourg et al., 2005). Refining this categorization by assessing finite strain and eclogite abundance separately allows to distinguish between deformation-related eclogitization and statically formed eclogitization (Zertani et al., 2019b).

The deformation-related eclogitization is characterized by the formation of eclogite-facies shear zones varying in width from millimeter to kilometer scale (e.g., Austrheim, 1987; Raimbourg et al., 2005; Zertani et al., 2019b). Field observations suggest that hydrous shear zones evolve from initial eclogite veins (e.g., Austrheim, 1987; Austrheim & Boundy, 1994; Boundy et al., 1992; Jamtveit et al., 1990; Jolivet et al., 2005). During ongoing eclogitization and penetrative ductile deformation, adjacent shear zones interconnect and form anastomosing networks with isolated granulite blocks (sharp transition from eclogite matrix to granulite blocks, Austrheim, 1987; Zertani et al., 2019b). The shear zones have a distinct foliation and are often accompanied by an alteration halo (<50% of eclogitization). Shear zone widening is caused by an increase of the abundance of eclogite (50%–90% of eclogitization). Ultimately, four major shear zones with a penetrative eclogite-facies foliation formed (e.g., Boundy et al., 1992, 1997; Fountain et al., 1994; Raimbourg et al., 2005; Zertani et al., 2019b).

Eclogites also form statically without associated ductile deformation. In this case, eclogites often form in finger-like structures originating from initial fractures into the granulite, commonly along the granulite foliation (<50% of eclogitization, Jamtveit et al., 2000). Ongoing static eclogitization causes the formation of isolated granulite blocks with a diffuse transition from eclogite to granulite, but without systematic disruption of the foliation and without consistent ductile shear direction (Zertani et al., 2019b). Finally, both transformation mechanisms form almost completely eclogitized areas.

All studied rocks occasionally indicate amphibolite-facies recrystallization, which either occurred shortly after and related to eclogite-facies metamorphism (Jamtveit et al., 2018b) or due to exhumation (Andersen et al., 1991; Jolivet et al., 2005; Kühn et al., 2002). Here, we focus on eclogitization.

Figure 1. (a) Conceptual lithospheric-scale cross-section at the time of collision of Baltica and Laurentia (orIO = oceanic rocks of the Iapetus Ocean; heM = hyperextended margin). (b) Schematic map indicating the outlines of northern Holsnøy to highlight its orientation and the tectonic setting during peak metamorphic conditions. Brittle deformation enables fluid infiltration, which, in turn, triggers the eclogitization. Subsequently, ductile deformation promoted the formation of eclogite-facies shear zones (green lines). (c) Map showing the location of northern Holsnøy northwest of Bergen, Norway (red box). (d) Geological map of northern Holsnøy showing the distribution of eclogite occurrences categorized with respect to their petrological transition (modified from Zertani et al., 2019a) and the location of the outcrops studied in detail and used in the model presented here (A and B).

3. Mapping and Petrological Methods

In order to derive the key parameters that control the geometry and progressive widening of eclogite-facies shear zones, we conducted detailed structural and lithological mapping of two representative outcrops with varying eclogite abundance to extract the geometry of the shear zone network. The outcrops were segmented into a grid with 2×2 m^2 sectors and first-order structural elements (e.g., foliation, lineation, fold axial planes, shear-sense, and fracture-sets), geometries of the eclogite-facies shear zones, and the occurrence of static eclogitization were documented in detail. Outcrops A and B cover 140 m^2 (35 sectors) and 320 m^2 (80 sectors), respectively. To support the structural maps, image data of a DJI Phantom 4 drone from the Centre of Earth Evolution and Dynamics at the University of Oslo was used complementary to the mapping.

Furthermore, 14 drill core samples were taken (length: 7–15 cm, diameter: 4.5 cm) out of which eight samples (unaltered, least affected by amphibolite-facies overprint) were selected for quantitative measurements of the major element composition of the rock-forming minerals. The measurements were performed using the *JEOL JXA 8800 SuperProbe electron microprobe microanalyzer* at the Freie Universität Berlin with an accelerating voltage of 15 kV, a beam current of 200 nA and a beam diameter of 1 μm for all analyzed minerals. Additionally, X-ray fluorescence analyses (XRF) of one pristine sample of each lithology were made with a *Panalytical Axios Advanced* spectrometer at the GeoForschungsZentrum Potsdam to obtain representative chemical bulk data for major and trace elements (Table S1). This data was used to verify that the exposed lithologies are representative in the regional context.

4. Geometry and Structural Relationship

4.1. Description of the Investigated Lithologies

The granulite-facies rocks have a distinct foliation defined by elliptic pyroxene-garnet coronas of which the long axis defines the lineation. The corona cores may consist of olivine and orthopyroxene (both commonly reacted out), surrounded by clinopyroxene (augitic to diopsidic) and garnet (e.g., Austrheim, 1987; Austrheim & Griffin, 1985; Austrheim & Robins, 1981). The granulite is coarse-grained (1–3 mm) and has a granoblastic microstructure. Microscopic investigations show that plagioclase often lined with small zoisite needles (a few μm in size), which indicate minor hydration of the granulite at eclogite-facies conditions. Additionally, granulite-facies pyroxene rims are sometimes surrounded by fine-grained omphacite.

Eclogites are fine-grained (<0.5 mm) and preserve remnants of the pyroxene-garnet coronas. The main mineral assemblage is garnet, omphacite, clinozoisite, kyanite, and accessory phases, for example, phengite, quartz, symplectites, and amphibole. The matrix minerals, mostly omphacite, have a shape preferred orientation. Garnets occur in rounded and partly elongated grains, ~0.5 mm in size. Omphacite grain size varies from 0.1 to 0.3 mm and the composition clusters around Jd_{54} (jadeite component) and they are not zoned (Table S1). The average matrix grain size is ~0.08 mm within the center of the shear zones, and ~0.05 mm at their rims, which was estimated by thin-section analysis using single grain measurements (about 30 randomly selected grains of each section). These measurements exclude the larger garnet crystals because they are not part of the matrix, which recrystallized during eclogite-facies metamorphism.

4.2. Outcrop Description

Outcrop A is characterized by a network of almost parallel and regularly spaced NE-SW-trending eclogite-facies shear zones that crosscut the granulite (Figures 2a and S1). The granulite foliation is well preserved and oriented ~230/70 (strike/dip) and at an angle of 60°–90° to the foliation of the eclogite (~320/65; Figures 2b and 3). The outcrop consists of 69% granulite, 17% eclogite-facies shear zones, and 14% statically formed eclogite, as was calculated via pixel-counting of the digitized petrological map, excluding the vegetation (Figure 2a). The eclogite-facies shear zones are between 10 and 110 cm wide (50 cm on average); measured perpendicular to their boundaries and have a top-to-the-SW sense of shear (Figure 3). They are well-ordered and in the context of the regional top-to-the-ESE kinematics on Holsnøy consistent with bookshelf-type deformation (e.g., Raimbourg et al., 2005). Where several shear zones interconnect the width increases. Locally, some eclogite-facies shear zones show remnants of the granulite foliation, which was slightly transposed by shearing (Figure 2a, bottom of the central shear zone).

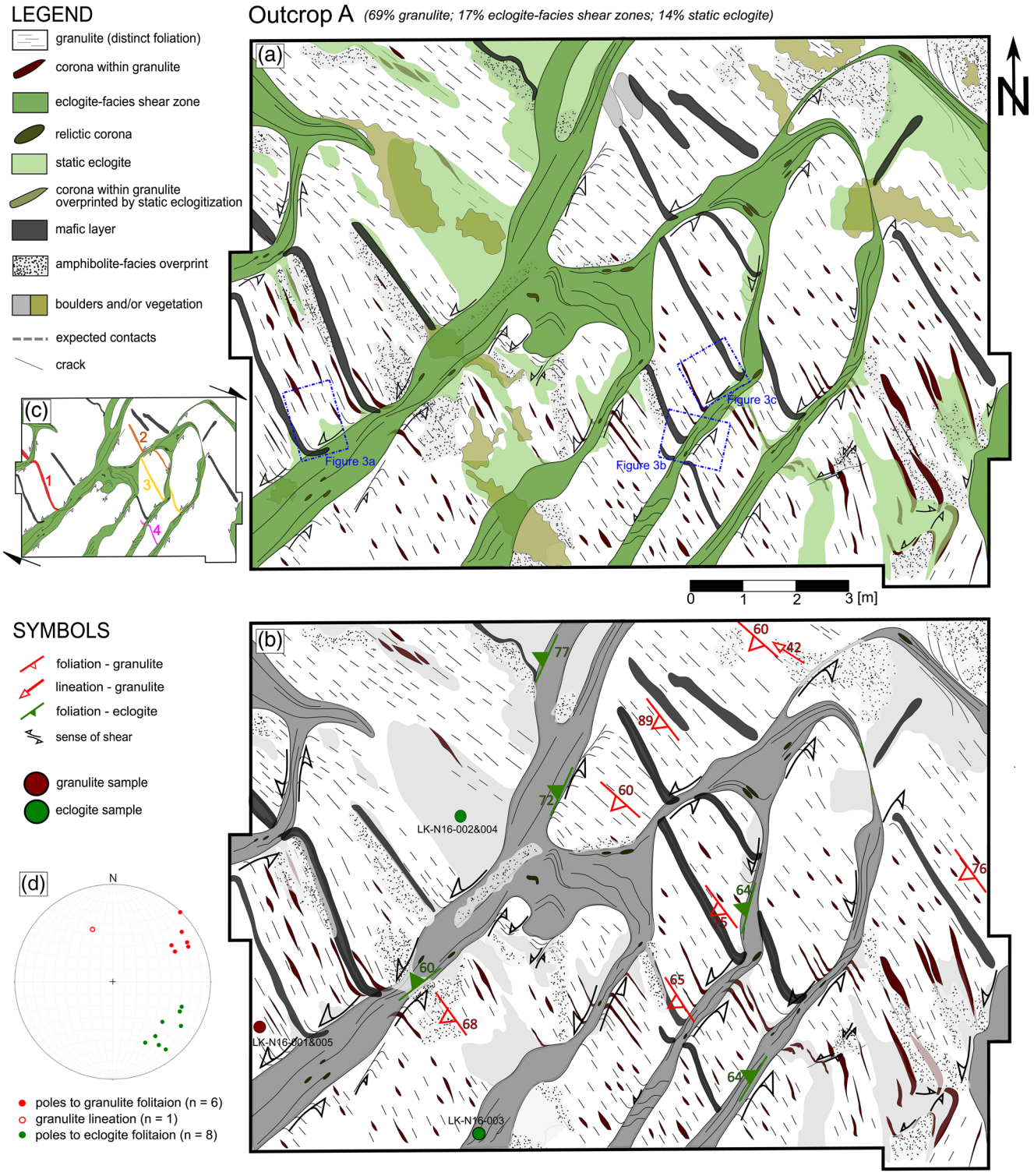

Figure 2. (a) Detailed lithological map of outcrop A. In addition, the amphibolite-facies overprint areas covered by vegetation are shown. Blue boxes indicate the location of the photographs in Figure 3. (b) Detailed structural map of outcrop A including foliation and lineation measurements and sample locations. (c) Simplified sketch of the petrological map illustrating the main kinematic relationship. The color-coded mafic layers are used as offset markers. (d) Plot with foliation and lineation measurements of the eclogite and granulite (Table S2; lower hemisphere, equal area projection).

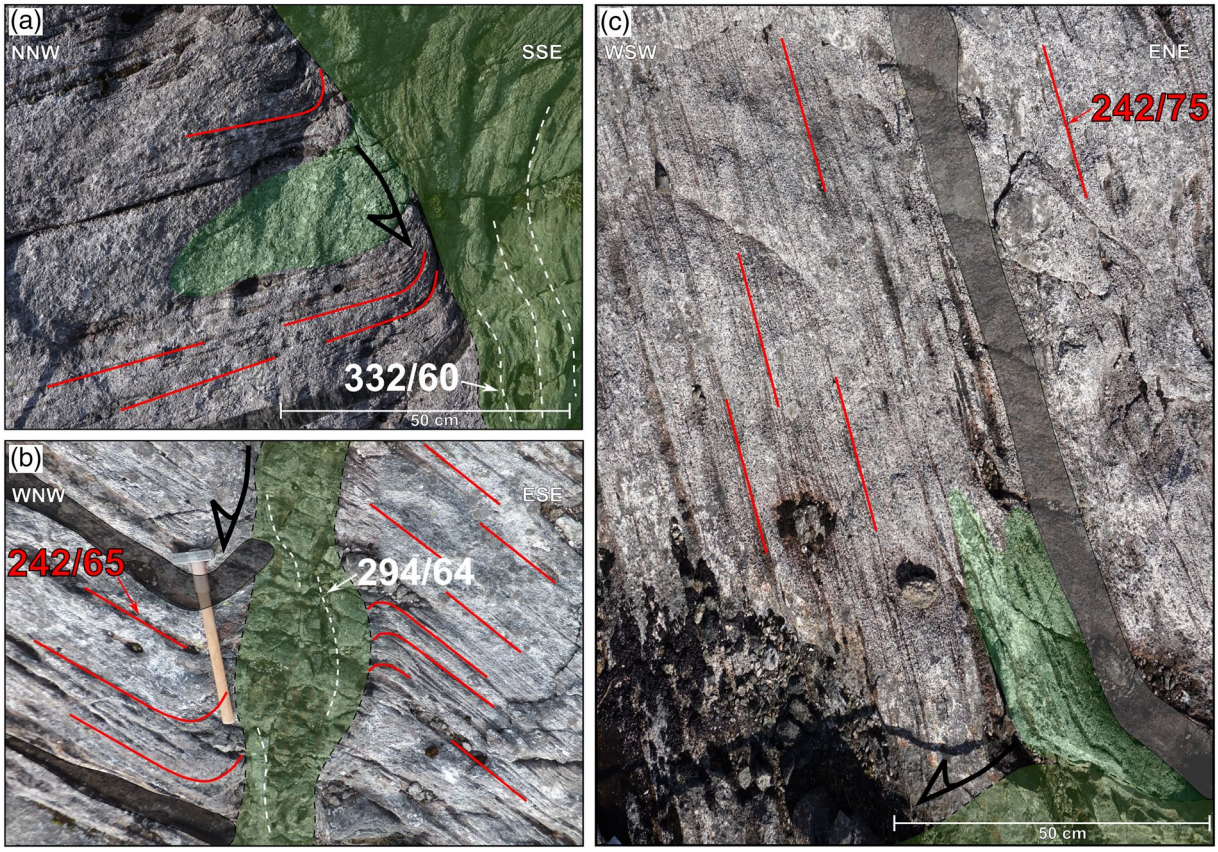

Figure 3. Photographs of representative small-scale eclogite-facies shear zones (top-to-the-SW; dark green) and patterns of static eclogitization (light green) from outcrop A. The eclogite foliation is given in white lines (azimuth/dip; a and b) and the granulite foliation is provided as red lines (average of all measurements ~230/70; b and c). Mafic layers (gray) as well as the granulite foliation are locally dragged into the eclogite-facies shear zones (a and b).

The shear zone spacing (measured between the centers of adjacent shear zones) divided by the shear zone width results in an average spacing-width-ratio of ~4.2. To assess the displacement of these eclogite-facies shear zones, we traced mafic layers within the granulite as offset markers (highlighted in Figure 2c). The flat surface of the outcrop precluded accurate measurements of the eclogite lineation. However, the eclogite lineation is close to horizontal with an orientation of 244/12 (strike/dip); reconstructed from one drill-core-sample. Taking this into account the average minimum displacement is ~0.3 m per shear zone. Using the mafic layers (1–4; Figure 2c) and the minimum displacement of each shear zone, we calculated shear angles (in 2-D). The corresponding average shear strain is $\gamma = 0.88$.

In outcrop B, the eclogite-facies shear zones are oriented E-W with a top-to-the-W, sense of shear (Figure S4). The outcrop consists of ~58% granulite, ~23% eclogite-facies shear zones, ~16% statically eclogitized rocks, and ~3% hydration fronts; excluding the vegetation, calculated by pixel-counting. The shear zones are on average ~1.3 m wide and are less ordered compared to those in outcrop A (Figure 4a). The granulite foliation (~085/60) is nearly perpendicular to the eclogite foliation, which varies in orientation between ~350/70 and ~170/60. The eclogite lineation plunges toward the west (~270/20; Figure 4b). Numerous interconnections between eclogite-facies shear zones result in a strong width variation along single shear zones and, additionally, shear zones are bulged (undulating shear zone boundaries). In some places, granulite blocks are completely surrounded by eclogite and rotated (up to 45°). These blocks are elongated with their longer axis parallel or subparallel to the eclogite foliation (Figures 4b and 3a). They are rotated because the surrounding eclogite has a lower effective viscosity than the granulites (e.g., Marques & Burlini, 2008). Other isolated granulite blocks seem interlocked and could not rotate unobstructed due to a space-shortage (Ramsay & Huber, 1983).

There are three different boundary types between eclogite-facies shear zones and the surrounding granulite: i) sharp transition from eclogite to pristine granulites (Figure 5a—upper left corner); ii) eclogite-facies shear

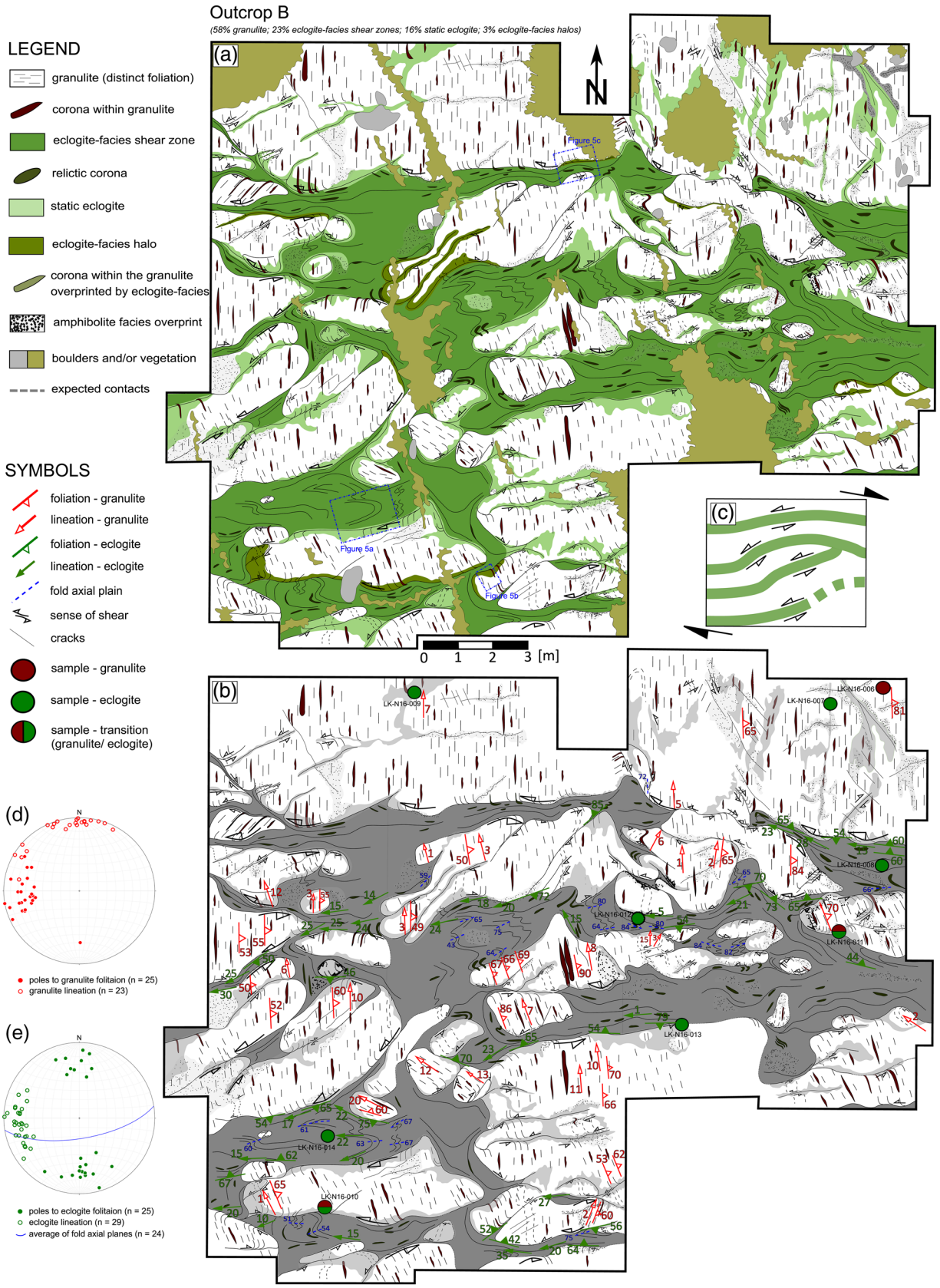
Outcrop B
(58% granulite; 23% eclogite-facies shear zones; 16% static eclogite; 3% eclogite-facies halos)
LEGEND
granulite (distinct foliation)
corona within granulite
eclogite-facies shear zone
relictic corona
static eclogite
eclogite-facies halo
corona within the granulite overprinted by eclogite-facies
amphibolite facies overprint
boulders and/or vegetation
expected contacts
SYMBOLS
foliation - granulite
lineation - granulite
foliation - eclogite
lineation - eclogite
fold axial plain
sense of shear
cracks
sample - granulite
sample - eclogite
sample - transition (granulite/ eclogite)
(a)
N
Figure 5c
Figure 5a
Figure 5b
0 1 2 3 [m]
(b)
LK-N16-009
LK-N16-007
LK-N16-006
LK-N16-008
LK-N16-012
LK-N16-011
LK-N16-013
LK-N16-014
LK-N16-010
(c)
(d)
poles to granulite foliaion (n = 25)
granulite lineation (n = 23)
(e)
poles to eclogite foliaion (n = 25)
eclogite lineation (n = 29)
average of fold axial planes (n = 24)

zone with static eclogitization patches following the granulite foliation, and iii) eclogite-facies shear zone with a thin halo (Figures 5b and 5c). The halo width (hf) and the width of the corresponding shear zone (sz) were measured to calculate their relationship (Table 1). On average, the halo corresponds to 12.6% of the total shear zone width (sz + hf). The spacing-width-ratio of outcrop B varies from ~1.6 to ~2.6. Consequently, in contrast to outcrop A, the shear zones of outcrop B are wider while having a similar spacing. Additionally, several eclogite-facies shear zones include folds, especially where they interconnect (Figure 5a). The folds range in amplitude from 5 cm to nearly 1 m.

Due to the observation that unambiguous offset markers are missing throughout the entire outcrop, and the difficulty in measuring the eclogite-facies lineation that is required to estimate the shear direction, no reliable quantitative estimate of the shear strain (γ) is possible. Therefore, we use first-order observations to estimate the shear strain. Several features suggest higher finite shear in outcrop B than in outcrop A. 1—the granulite foliation is only locally deflected along the shear zones in outcrop A (Figure 2a), while some granulite blocks are rotated up to 45° in B (Figures 4a and 5a); 2—some shear zones in outcrop A show remnants of the granulite foliation with limited transposition in the shear direction (Figure 2a), while outcrop B develops a penetrative shear-parallel eclogite-facies foliation within the shear zones, implying that a substantial amount of strain was accommodated during crystallization; 3—the location of the two outcrops in the larger-scale strain pattern (Figure 2d) differ. Even though both outcrops are located within larger granulite blocks associated with the deformed eclogite breccia unit (Figure 1d), A is located at the side of a larger low strain domain, while B is at the tip of a near km-wide major eclogite-facies shear zone.

5. From Field Observation to Numerical Simulation

We extracted the main observations from the two mapped outcrops and used them as constraints for the numerical models. One main observation is that the geometries of the shear zone networks vary. While outcrop A features a few, well-ordered, and parallel eclogite-facies shear zones, the network of outcrop B is more chaotic. Here, the shear zones have a bulged geometry, which potentially arises due to a larger finite deformation (higher finite shear). Furthermore, the shear zones in outcrop B are more than twice as wide (on average 1.3 m) as the ones in A (on average 0.5 m) while their spacing is similar. Consequently, outcrop B has a higher abundance of eclogite. It is therefore likely that the structures preserved in outcrop A reflect an earlier stage of the shear zone evolution than outcrop B, as is also corroborated by the relative strain estimate discussed in section 4.2. Thus, we assume that they represent two successive substages of the deformation-related eclogitization (Figures 6c and 6d). We suggest an evolution of the structures as shown in Figure 6: a) Fractures allow an external fluid to infiltrate. b) The introduction of the fluid leads to the formation of an eclogite-facies mineral assemblage. The presence of the fluid, the ongoing reactions, and the grain size reduction result in weakening of the rock enabling ductile deformation. c) The shear zones rotate during ongoing ductile deformation. This step illustrates the observed structures of outcrop A with bookshelf-type deformation and sinistral eclogite-facies shear zones. d) Even though the shear zones rotate subparallel to the shear direction, they widen (outcrop B).

5.1. Basics of the Mumerical Simulations

Using numerical simulations, we evaluate how the fluid budget affected the shear zone geometry and the width variations observed in the field, and if the finite geometry is driven by pressure gradients (lower at shear zone rims, higher in the shear zone center), which may have controlled the distribution of the fluid (Moulas et al., 2014, 2019). We use a simplified geometric configuration to evaluate the effect of dextral simple shear (consistent with the regional shear direction) and fluid infiltration in an initially dry system containing fluid-filled low-viscosity zones. The real fluid budget that was involved and the timescales of deformation and fluid migration are unclear. Nevertheless, numerical simulations can be used to constrain the dominantly active physical processes in order to better understand the main mechanisms involved dur-

Figure 4. (a) Detailed lithological map of outcrop B. Blue boxes indicate the locations of three representative photographs. (b) Detailed structural map of outcrop B. (c) Simplified sketch indicating the orientation of the four main shear zones with respect to regional kinematic reference frame (top-to-the-ESE; Raimbourg et al., 2005). (d) Plot of the granulite foliation and lineation measurements (lower hemisphere, equal area projection). (e) Plot showing foliation and lineation measurements of the eclogites as well as eclogite fold axis (summary of structural measurements in Table S2).

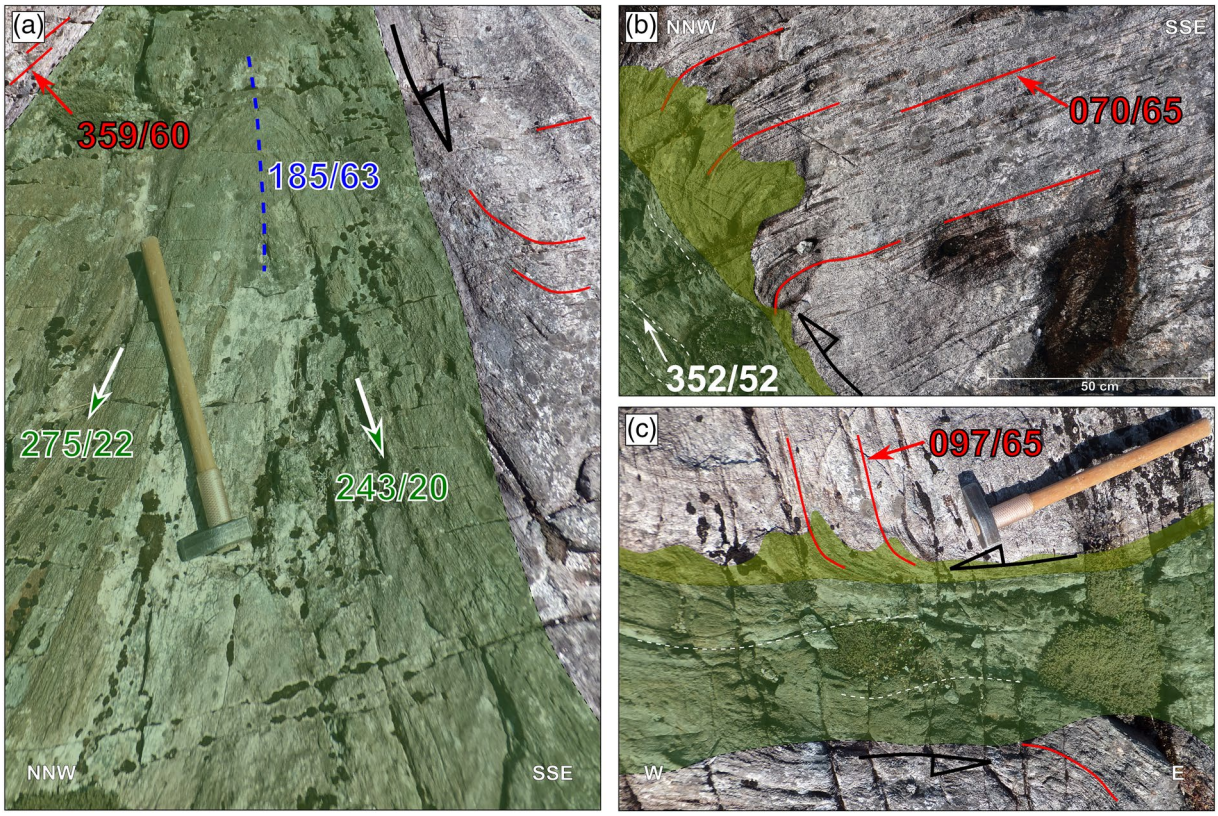

Figure 5. Photographs of three representative locations from outcrop B (locations given in Figure 4a). (a) Fold within eclogite-facies shear zone (fold axial plane in blue, eclogite lineation in green) surrounded by granulite (granulite foliation in red). Note the highly rotated granulite block in the upper left corner and the only location with dextral sense of shear (right). (b and c) Sinistral eclogite-facies shear zones (dark green) with a thin halo (olive-green) to the right. The granulite foliation (red) is almost perpendicular to the eclogite-facies foliation (white).

ing shear zone evolution. Hence, we investigate whether deformation or fluid infiltration has the larger impact on producing the observed geometries and causes shear zone widening instead of thinning, due to subshear parallel orientation of the eclogite-facies shear zones.

Our mathematical model is based on continuum mechanics. We consider slow (no inertial forces), linear-viscous flow of incompressible media in the absence of gravity (Pollard & Fletcher, 2005). The equations used to model the viscous deformation are described in Räss et al. (2017). The hydration process is described by a simple parametrization that utilizes a diffusion equation to mimic fluid infiltration. Using a diffusion equation to model the first-order features of fluid infiltration is reasonable, because chemical diffusion, porous fluid flow, and coupled fluid flow with chemical reactions are all effectively diffusion processes (see Lasaga, 1986, 1998 for details). Also, diffusion has been applied already to study fluid influx into stressed dry granulites for the case of static eclogitization (e.g., Jamtveit et al., 2000). The fluid infiltration, or hydration, process is described by the following diffusion equation:

$$\frac{\partial C}{\partial t} = \frac{\partial}{\partial x_i}\left(D \frac{\partial C}{\partial x_i} \right) \tag{1}$$

where C is a compositional variable (dimensionless) monitoring the amount of hydration in the rock (relative fluid content). The initial value of C for granulite is 0 (no fluid present) and 1 for the eclogite-facies shear

Table 1
Representative Halo Width Measurements of Outcrop B and the Corresponding Shear One Width

Shear zone width (sz) (m)	Halo width (hf) (m)	$\frac{hf}{hf+sz}\cdot 100\%$ (%)
1.04	0.17	14.1
1.50	0.22	12.8
0.44	0.050	10.2
0.38	0.047	11.0
0.47	0.083	15.0
		Ø 12.6

Note. The percentage of width-relation between the halo, which is induced by fluid infiltration and hence, hydration and the shear zone width is quantified.

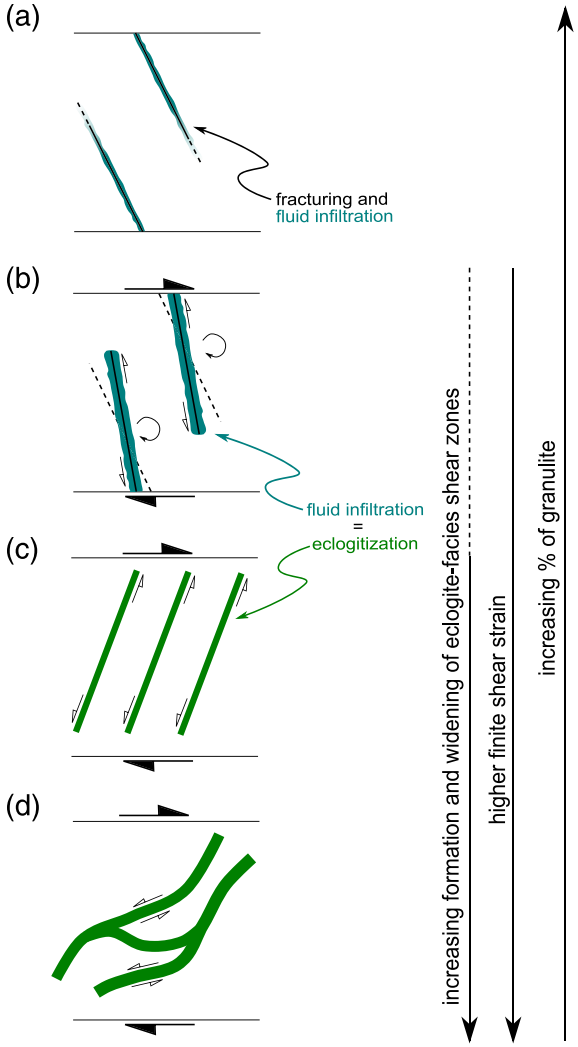

Figure 6. Sketch to indicate the evolution of the observed structures with respect to the regional kinematics (dextral sense of shear). (a) Fractures provide fluid pathways. (b) Ongoing eclogitization, ductile deformation, and rotation due to dextral shear. (c) Sketch resembling the situation in outcrop A, with parallel and regularly spaced eclogite-facies shear zones. (d) Further widening of the shear zones leads to mutual connection between single shear zones and the development of more chaotic shear zone network.

zones (saturated with fluid). The symbol t represents the time (in s), D is the effective diffusion coefficient (in m^2/s) and x_i is the spatial coordinate (in m) in the\ ith direction (Einstein's summation rule on repeated indices apply). The effective diffusion coefficient is constant in the model domain. To obtain scale-independent results, the system of equations was formulated in a nondimensional form. Based on previous studies, we assume that the viscosity of the eclogites for the considered conditions is ~1 order of magnitude less than the viscosity of the granulites (cf., Labrousse et al., 2010; Terry & Heidelbach, 2006). To calculate the effective viscosity of the partially hydrated rock (i.e., when $0 < C < 1$) we considered different mixing schemes between the weak (eclogite) and the strong (granulite) viscosities based on the amount of hydration (C). The two mixing schemes that were used are the arithmetic and the harmonic averaging (see Text S7, supporting information). Both schemes have been considered in geodynamic studies and they are used as limiting cases for effective rheology (Karato, 2008). In both mixing schemes the nondimensional fluid content is used as a weighting factor. Thus, the fully hydrated zones ($C = 1$) have the viscosity of eclogite, and the dry surrounding matrix ($C = 0$) has the viscosity of granulite. A partially hydrated domain has an intermediate viscosity. We utilized the granulite viscosity μ_m (in Pa·s), background shear strain rate $\dot{\varepsilon}_b$ (in s^{-1}, simple shear) and initial width of shear zones L (in m) as characteristic scales for the nondimensionalization of the equations. By introducing these parameters, we define a relative (dimensionless) diffusion coefficient ($\frac{D}{L^2 \cdot \dot{\varepsilon}_b}$) that was used in Equation 1. To solve the system of equations, we used the open access M2Di solver (Räss et al., 2017). M2Di solves velocity, pressure, and stress for the applied simple shear velocity boundary conditions and the applied spatial viscosity distribution (see Text S7, supporting information for details). M2Di was further coupled to a finite-difference implicit solver for the hydration (diffusion) equation (Equation 1). The spatial distribution of the effective viscosity thus evolves in time as a result of diffusive hydration (Equation 1) and the material properties are advected by the calculated velocities. To track the material interfaces (strong/weak initial lithologies) during deformation, we use a level-surface approach as in Moulas and Schmalholz (2020).

5.2. Initial Model Configuration Based on Field Observations

Orientation of the shear zones: Our working hypotheses is that a simple geometry developed into a complex network of eclogite-facies shear zones within a rigid granulite matrix (Figure 6). For simplicity, we consider two bands representing the initial distribution of the later eclogite-facies shear zones (lithology 1; Figure 6a) that are surrounded by the granulite matrix (lithology 2). This initial geometrical configuration is based on the assumption that the bands (weak zones) rotated with respect to the regional strain axis, as indicated in Figure 6. Therefore, this assumes that the shear zones were oriented like the fractures shown in Figure 6a at the onset of ductile deformation.

Kinematics: Deformation is related to the regional sense of shear (top-to-the-ESE; e.g., Raimbourg et al., 2005) and, hence, implemented as dextral simple shear in the model. The applied finite shear strain is given in %, and 100% of strain is equal to $\gamma = 1$. Due to the mafic layers, outcrop A defines a minimum γ of 0.88, which accordingly corresponds to 88% strain (for detailed description see Section 5).

Shear zone width-relationship: The spacing-width-ratio decreases from outcrop A to B, with increasing eclogitization. For the model setup, we use an initial spacing-width-ratio of ~3.

The predefined characteristics, for example, viscosity of each lithology and spacing-width-ratio are kept identical in every simulation. Since we solve the equations in nondimensional form, the results are scale-independent and can be upscaled from hand-specimen to regional scale. This is suitable for further investigations, because field observations suggest that all geometries and associated mechanisms are present at various scales (e.g., Zertani et al., 2019b).

A further requirement of our numerical simulations is the application of realistic boundary conditions. Kinematic boundary conditions (e.g., velocities at the model boundaries) would result in unrealistic stress concentrations at the material interfaces on the boundaries. To avoid these artificial stress concentrators, the shear zones are assumed to be finite and, consequently, surrounded by the considered model volume. Therefore, the shear zones do not touch the model boundaries (Figure 9).

5.3. Results and Interpretation of The Numerical Simulations

Since the amount of hydration (C) affects the viscosity and therefore the mechanical evolution of the shear zones, we generated three numerical models to identify the key parameters that have the largest impact on a weak zone and its geometric evolution. Our first model is the reference case, which considers the deformation (dextral shear) without any effect of fluid migration. Two end-member cases were considered with respect to the conservation of the fluid content. The first case (Case A) considers that the amount of fluid is conserved and therefore the migration of the hydration front of the shear zone would lead to a wider distribution of the available fluid (Figure 7). This implies that even though the shear zone centers were fully saturated initially, they become drier in the sense of fluid per reacted area as the model evolves. The second case considers that the shear zones were kept saturated during deformation (Case B). In contrast to Case A, the core of the shear zone in Case B is always fluid saturated, which means there is always sufficient H_2O to keep the hydration processes ongoing, that is, C is always 1 inside the initial volume of the shear zone. Both cases are possible end-member scenarios, which would favor the formation of wider shear zones during progressive deformation. In both cases, the fluid diffuses from the shear zone's core toward the (initially) dry rock. On the first order, the width of the hydration front of the shear zone depends on the value of the effective fluid diffusion coefficient (D) and not on the particular choice of the boundary conditions.

During the simulation, four parameters were monitored. These are as follows: i) the pressure (P); ii) the second invariant of the deformation-rate tensor ($\dot{\varepsilon}$); iii) the effective viscosity (μ); and iv) the amount of hydration (C). The pressure (P) is the mean stress of the solid defined as positive for compression. In an incompressible model with kinematic boundary conditions, such as the one used here, the pressure is defined up to a constant value. This constant value is the mean stress of the matrix in the far-field region. Therefore, the pressure values that are shown are the deviations from the mean stress of the matrix due to the presence of viscosity heterogeneities (cf., Moulas et al., 2014). Since we solved the system in nondimensional form, the reported parameters have been normalized using the matrix viscosity (μ_m) and the background (far-field) strain rate ($\dot{\varepsilon}_b$) as independent scales.

We applied 132% of strain ($\gamma = 1.32$), which is almost one-and-a-half times more than the minimum estimates of outcrop A. As mentioned, we assume outcrop B to be sheared more extensively than A. The results of the initial case show that the deformation without considering a fluid infiltration has no effect on shear zone widening. To identify the most appropriate relative diffusion coefficients (D) for the fluid influx, we tested various ones for Cases A and B applying both mixing schemes (Figure 8). In our study, based on the independent scales that were used to calculate the effective diffusion coefficient, a dimensionless diffusion coefficient of 0.01 corresponds to a case where $\frac{D}{L^2 \cdot \dot{\varepsilon}_b} = 10^{-2}$. Considering an initial shear zone width of $L = 1$ m and a background strain rate of $\dot{\varepsilon}_b = 10^{-13}\mathrm{s}^{-1}$ (based on Labrousse et al., 2010), the associated effective diffusion coefficient would be $D = 10^{-15}\frac{\mathrm{m}^2}{\mathrm{s}}$. As shown in Figure 8, we tested values for an effective diffusivity range from $D = 10^{-14}\frac{\mathrm{m}^2}{\mathrm{s}}$ to $D = 10^{-19}\frac{\mathrm{m}^2}{\mathrm{s}}$. Higher values cause an immediate eclogitization of the entire system and lower values prevent a hydration of the shear zone boundaries. Considering different background strain rates from $\dot{\varepsilon}_b = 10^{-13}\mathrm{s}^{-1}$ to $\dot{\varepsilon}_b = 10^{-15}\mathrm{s}^{-1}$ and using the halo and shear zone width rela-

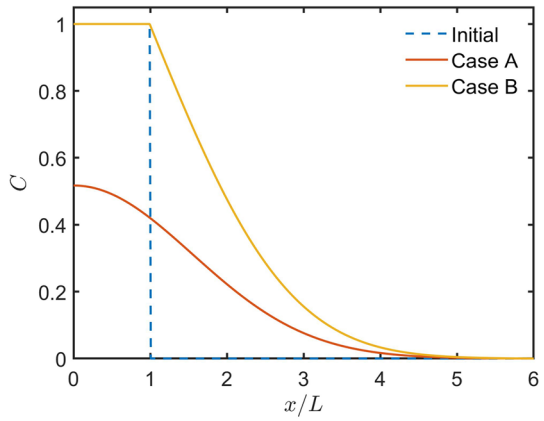

Figure 7. Example of one-dimensional diffusion process that describes the diffusion of fluid in the vicinity of a planar shear zone. The diffusion of fluid occurs from the center of the shear zone (left) to the surrounding ($x/L > 1$). The model is symmetric with respect to the x-axis and the horizontal distance x has been normalized to L, which is the shear zone's half width. In Case A, (conservative fluid amount) there is no fluid flux at the center of the shear zone ($x/L = 0$) and the total fluid content is conserved. In Case B, the shear zone is always kept saturated ($C = 1$). Note that both models predict the hydration of the shear zone boundaries ($x/L > 1$).

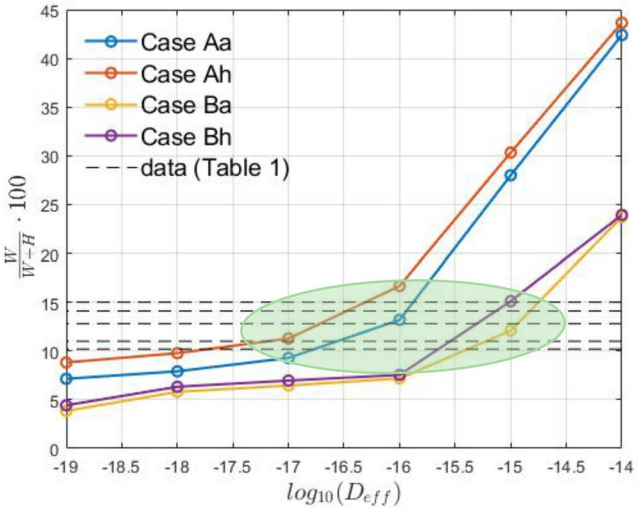

Figure 8. Results of the halo width/shear zone width relationship (y-axis) caused by the implementation of different dimensionless diffusion coefficients (x-axis; log of the effective diffusivity D) for Cases A and B with arithmetic and harmonic averaging. The green ellipse indicates the overlap of the field data (see Table 1) with the results of the numerical simulations, which suggests an effective diffusivity ranging from $D = 10^{-15}\,\frac{m^2}{s}$ to $D = 10^{-17}\,\frac{m^2}{s}$ for the mapped structures.

tion of the observed structures (Table 1) and the ones of Cases A and B, Figure 8 suggests that an effective diffusivity between $D = 10^{-15}\,\frac{m^2}{s}$ and $D = 10^{-17}\,\frac{m^2}{s}$ is most appropriate to fit the field data.

Since the width of the shear zones increased during the hydration process, we define the "effective shear zone" as the area (in two dimensions) where the viscosity is 10 times smaller than the matrix viscosity $\left(\frac{\mu}{\mu_m} = 0.1\right)$. The hydrated halo is defined as the area (in two dimensions) where the viscosity varies between 0.2 and 0.9 of the matrix viscosity. The thickness of the shear zone and the halo are measured perpendicular to the shear zone boundaries (Figures 9-Case A and B). In Case B, where a continuous fluid infiltration is implemented (i.e., shear zone centers are always saturated; $C = 1$) the produced halos are smaller than in Case A (Figure 8), but the shear zone width $\left(\frac{\mu}{\mu_m} = 0.1\right)$ increases during deformation (Figure 9).

Figure 9 shows the initial conditions used for the simulations and the results of the three numerical models with arithmetic and harmonic averaging. Line 1 displays the evolution of the dynamic pressure within the eclogite-facies shear zones. The dynamic pressure is highly affected by deformation and depends on the orientation of the shear zones with respect to the overall boundary conditions (stretching and shortening direction). The dynamic pressure is distributed in the same way in each of the three models. Dextral shearing imposes oblique directions of maximum shortening and stretching. Here, the eclogite-facies shear zones are viscous weak inclusions, surrounded by a strong matrix. The shear zones are underpressurized (negative dynamic pressure) when they are oriented parallel to the main direction of shortening (Figure 9, initial conditions). Once the shear zones are oriented at a ~45° angle to the main direction of shortening, the dynamic pressure is nearly equal to the matrix mean stress. When the shear zones are almost parallel to the main direction of stretching (after 132% of strain) the dynamic pressure is positive. The pressure variation which is detected within the shear zones (visible at 132% of strain), is a consequence of the force balance and the material heterogeneity. If one region exhibits higher deviatoric stress, the adjacent regions exhibit higher pressure to ensure that force balance is maintained, that is, a continuous total normal stress (i.e., mean stress plus deviatoric stress) across material boundaries. The free availability of fluid due to continuous fluid infiltration has the strongest effect on bulging (Figure 9—Case B) because the fluid and hence, the eclogitization, follows low-pressure regions. The results show that deformation without an incorporated fluid (Figure 9—column 2) has a high effect on the dynamic pressure variations but is almost negligible for widening and geometric modifications of the eclogite-facies shear zones.

The strain rate evolution of the three models is identical (Figure 9—Line 2). During dextral shearing, the strain rate increases in the outer rims of the shear zones, which induces stress concentrations. When stress increases locally, it drops in adjacent regions to maintain the force balance (Figure 9—2'). Viscosity is assumed to be constant, if no fluid infiltrates (Figure 9—Lines 3 and 4). If the amount of fluid increases the viscosity decreases, which eventually leads to weakening of the granulite and results in the transformation to eclogite. Once a fluid is introduced a hydration halo forms (Figure 9—Cases A and B). Within this halo the viscosity

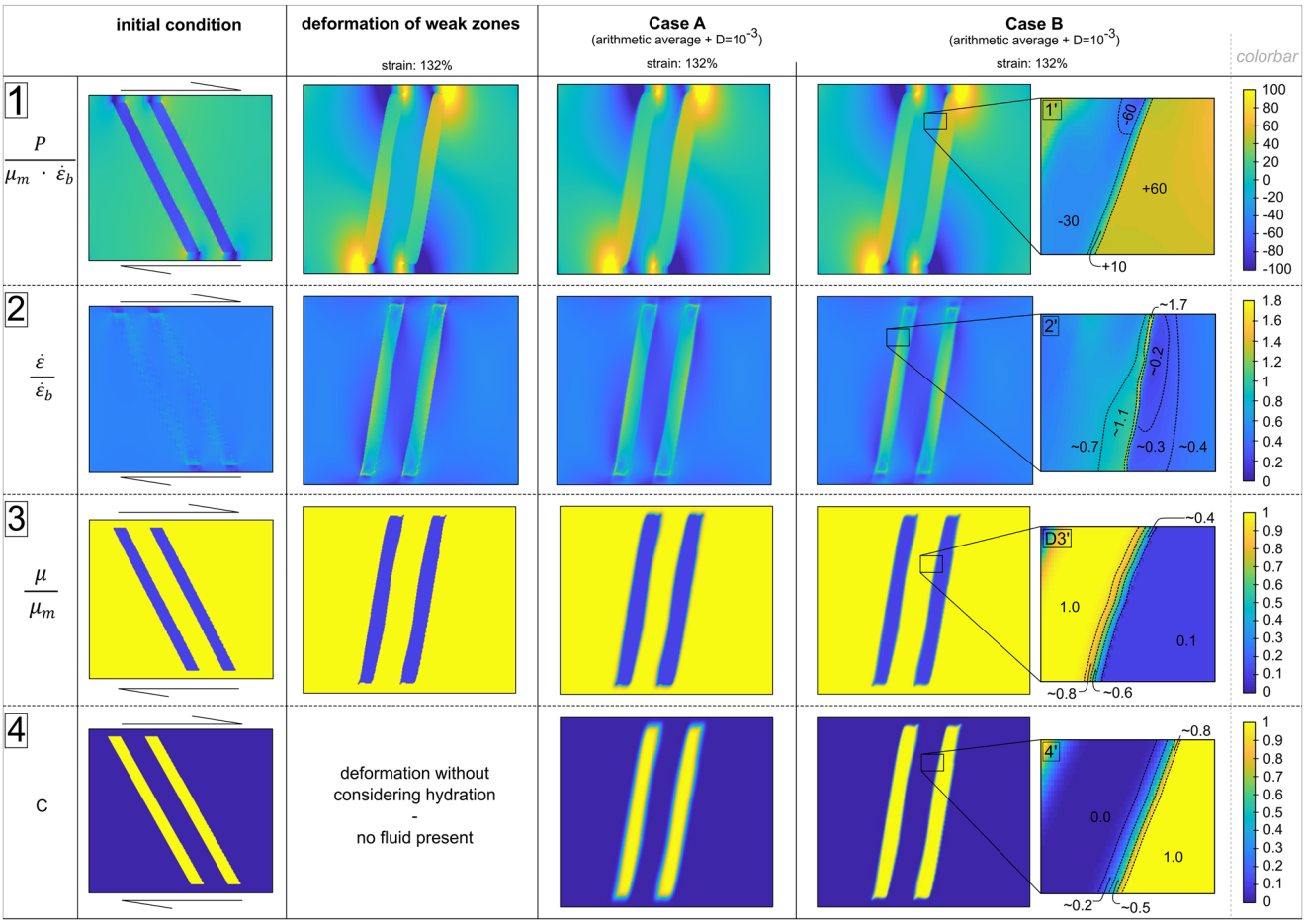

Figure 9. One result compilation of the numerical simulations of the three models generated during this study. The figure is segmented into four columns: (1) Simplified initial geometry used for all simulations (0% of the finite shear strain). (2) Reference model considering deformation, implemented as dextral shearing, without fluid-rock interaction (132% of strain). (3) Case A assumes a constant fluid amount coupled with deformation ($D = 10^{-3}$). (4) Case B introduces a continuous fluid infiltration (free fluid) coupled with deformation ($D = 10^{-3}$). Additionally, the results for the calculated parameters with arithmetic averaging are shown in line 1–4: (1) dynamic pressure $\frac{P}{\mu_m \cdot \dot{\varepsilon}_b}$; (2) strain rate $\frac{\dot{\varepsilon}}{\dot{\varepsilon}_b}$; (3) viscosity $\frac{\mu}{\mu_m}$, and (4) relative fluid content C. Every numerical model is in nondimensional form and hence, scalable. The most appropriate effective diffusivity is around $D = 10^{-16}\,\frac{\mathrm{m}^2}{\mathrm{s}}$ (shown here) Exemplary, the close-ups in column D display the details within local variations of the calculated parameters.

of the host rock is reduced. The rotation of the shear zones seems to be negligible at least for the dynamic pressure of the halo because it is nearly the same as the matrix mean stress.

6. Discussion

Eclogitization on Holsnøy was initiated by the interplay of deformation and fluid infiltration (e.g., Austrheim, 1987; Austrheim & Griffin, 1985; Boundy et al., 1992; Jamtveit et al., 1990; Jolivet et al., 2005; Raimbourg et al., 2005). Brittle deformation and fragmentation of the granulite host rock due to seismic activity enables the fluid to enter the system (e.g., Incel et al., 2019; Jamtveit et al., 2018b; Putnis et al., 2017). Subsequently, fluid-rock interaction coupled with ductile deformation promotes eclogitization of the preexisting granulites evolving via eclogite-facies shear zone networks and ultimately results in completely eclogitized areas (Austrheim, 1987; Jolivet et al., 2005). Detailed mapping of two representative sets of shear zones was the basis for simple numerical models. It was possible to reproduce first-order characteristics of the shear zone widening and the main geometrical features as extracted from field observations. The pressure and strain rate evolution are described during deformation of the shear zones and as a function of the viscosity

of the involved lithologies. Viscosity variations themselves depend on the presence of a fluid. Using the relationship of these parameters, we reconstruct how deformation and fluid-infiltration enables progressive eclogitization via shear zone widening on meter-scale structures.

6.1. Evolution of The Eclogite-Facies Shear Zones

The initial model setup (Figure 6a) is based on our field observations coupled with findings of other studies, for example, Austrheim (1987); Jolivet et al. (2005) and Raimbourg et al. (2005) and represents the starting point of the deformation. The orientations of the shear zones of the two outcrops differs by ∼45° (outcrop A NE-SW, and outcrop B E-W). Fusseis et al. (2006) suggests that the development of similar shear zone networks might be a result of host- and step-over shear zones without requiring any rotation. However, we infer a rotation of the eclogite-facies shear zones based on the concept of bookshelf style deformation, which is supported by the observations of Raimbourg et al. (2005) and Zertani et al. (2019b) as well as our own field observations. Furthermore, we suggest fractures to be the precursor structures for fluid infiltration. With respect to the far field stress of Holsnøy the assumed initial fracture orientation (Figure 6a) agrees with the concept of antithetic Riedel-type (R′) structures.

A fundamental limitation of transferring the natural geometric evolution of the shear zones to numerical simulations is the continual formation of new eclogite-facies shear zones, which is assumed to be typical for the structures of Holsnøy (e.g., Austrheim, 1987; Raimbourg et al., 2005). Some parallel eclogite-facies shear zones develop into a less ordered shear zone network. New shear zones form continuously and already existing ones connect (e.g., Jolivet et al., 2005). This scenario is repeated over a certain period and hence, the shear zone network is formed, widens, and progressively transforms the entire granulite host rock to eclogite. The ongoing and dynamic process has a strong impact on the shear zone geometries, but it is a complex task to reproduce this process in numerical simulations and beyond the scope of our study. Therefore, the shear zone geometries modeled here are limited by several simplifications. However, we could reproduce marked similarities to the observed eclogite-facies shear zone system, for example, bulging, and widening (Figure 9).

6.2. The Effect of Introducing a Fluid

When deformation is coupled with fluid infiltration in the simulations, the shear zones widen and bulge. The evolution of the model resembles, on the first order, the geometric evolution we infer for the mapped structures of both outcrops. With regard to the amount of eclogitization, the initial geometrical model configuration consists of ∼14% eclogite, calculated by pixel-counting where effective viscosity of 1.0 is considered to be eclogite. The outcome of Case A (limited fluid supply, Figure 9) consists of ∼16% eclogite, which is slightly higher than the initial configuration and similar to the mapped eclogite abundance of outcrop A (shear zones = 17%, Figure 2). The results of Case B (unlimited fluid supply, Figure 9) show an increase in the abundance of eclogite to ∼21% (viscosity pixels of 1.0), which is similar to the one of outcrop B (shear zones = 23%, Figure 4). Simulations for Cases A and B produce a hydration halo and shear zone width relationship close to the one observed in outcrop B (Figure 8). During the simulations, eclogitization is detected by the change of the effective viscosity, which decreases if granulite is transformed into eclogite. This viscosity is controlled by the amount of hydration, C which itself is a function of how efficient the fluid infiltrates the nonreacted rock. Comparing the halo and shear zone thicknesses relationship in both cases the results indicate that the reaction halo is less pronounced in Case B (Figure 8). This supports the field data of the mapped outcrops because the fewest shear zones have thick and clearly pronounced hydration halos (Figures 2 and 4). Additionally, only Case B produces shear zone boundaries with pronounced undulations. Based on our results, it is evident that amount of infiltrating fluid must have been substantial to form geometries, as those mapped in the field. This substantial volume of fluid infiltration can be achieved either by a continuous supply or by repetitive pulses of fluid infiltration. Such pulses have been proposed for shear zones exposed in Lofoten (northern Norway), where similar crustal rocks were locally transformed into eclogite (Fournier et al., 2019). There, however, viscously deforming shear zones did not widen and are restricted to the width of their precursor (Menegon et al., 2017). Additionally, the volume of fluid available during such pulses is limited by the volume of the transiently forming porosity during the fluid-induced reaction (e.g., Taetz et al., 2018) and the

volume of eclogitization in our Case A is insignificant compared what can be observed in the field. Considering that the shear zones widen up to a few 100-m width and even expel fluids that produce static re-equilibration on substantial scales (Austrheim, 1987; Jamtveit et al., 2000; Jolivet et al., 2005; Zertani et al., 2019b) we suggest that the fluid supply must have been continuous for the duration of the eclogitization process. However, both outcrops feature widened and less widened parts within one single shear zone. We suggest this is possibly the result of an anisotropic stress state accompanied with the start of static eclogitization (Jamtveit et al., 2000) or some parts are either more sensitive to fluid infiltration promoting eclogitization and hence, widening, or to stretching, which causes thinning. Hence, the effect of stretching is possibly tempered by the effect of fluid-rock interaction. This assumption could be a reason for the high width variation within single shear zones. In our model, fluid infiltration is controlled by an effective diffusivity, D. In this first quantitative study, we identified an effective diffusivity of around $D = 10^{-16}\,\frac{\mathrm{m}^2}{\mathrm{s}}$ for our medium, which provides a width to halo relationship close to the observed one. This effective diffusivity mimics various natural diffusion-type processes in rocks including, for example, grain boundary diffusion, lattice diffusion, and transiently dissolution and precipitation enhanced diffusion. Published experimental diffusion coefficients for oxygen, H_2O and light element diffusion within common minerals (through the crystal lattice) are expected to be slower, around $D = 10^{-16}\,\frac{\mathrm{m}^2}{\mathrm{s}}$ (Brady & Cherniak, 2010), than grain boundary diffusion, and especially through grain wet grain boundaries and fluid filled porosity, $D = 10^{-12}\,\frac{\mathrm{m}^2}{\mathrm{s}}$ (Dohmen & Milke, 2010; Taetz et al., 2018). According to Dohmen and Milke (2010), slow diffusivities highly influence the effective diffusion of the entire medium and work as limiting factors. The best-fitting effective diffusivities in our model agree, within an order of magnitude, with established diffusion coefficients for polycrystalline materials, which suggests that the modeled fluid transport by diffusion is indeed an important process during natural shear zone widening.

6.3. Pressure Variations Within The Shear Zones and Induced Fluid Flow

The results show that deformation, which is generated by dextral shear, has a strong effect on the dynamic pressure and stress evolution. Variations in the pressure and stress field are functions of two parameters: i) the viscosity contrast between the involved lithologies and ii) the orientation of the weak viscous shear zones with respect to the far-field stress. The shear zones are underpressurized when they are oriented parallel to the main direction of shortening and overpressurized, when they are parallel to the main direction of stretching. These pressure changes during rotation imply that the weak zones first absorb and then expel the fluids toward the host rock or distribute the fluid within the shear zones network. Accordingly, the pressure-fluctuations would act as a (fluid) pump. The fact that the product of the fluid-rock-interaction (eclogite) is at least transiently weaker than the reactant assemblage is possibly controlling this mechanism. Indeed, the fluid is likely to be delivered by an external fluid source (Andersen et al., 2012; Jakob et al., 2019), which is probably limiting this pumping-mechanism because we assume an unlimited fluid supply to keep the shear zone centers saturated (Case B)

We do not calculate fluid pressure in this study. Nevertheless, the calculations result in pressure variations that warrant speculation about their possible implications for the regional-scale eclogitization within and along the hydrous shear zone network. Fluid transport within active shear zones may be enhanced by creep cavitation processes (e.g., Fusseis et al., 2009) or in the absence of deformation during fluid-driven metamorphism (static eclogitization) fluid transport might be governed by diffusio-osmotic fluid flux in reaction-induced pore structures (e.g., Plümper et al., 2017). However, to allow the eclogitization of a regional-scale shear zone network, like the one on Holsnøy (Figure 1), it is required to disperse the reaction-driven fluid over the entire volume of the affected crust. Spatially distributed pressure fluctuations, causing recurring fluid pulses within an evolving shear zone network would enhance the fluid transport efficiency of the system. In turn, fluid transport promotes deformation by inducing rock weakening and consequently, creating new pressure fluctuations thus, potentially generating a self-reinforcing system.

7. Conclusion

In this study, we configure a simple numerical shear zone model with observed strain estimates, geometries and boundary conditions based on detailed mappings of two outcrops on Holsnøy representative for beginning eclogitization in a fluid-mediated shear zone network. We compare the mapped ratios of halo width to shear zone width with the numerical results. The numerical simulations show that a continuous fluid supply reproduces best the first-order shear zone geometries and ratios of halo to shear zone width observed in the field. An effective fluid diffusion coefficient ranging from $D = 10^{-15}\,\frac{m^2}{s}$ to $D = 10^{-17}\,\frac{m^2}{s}$ is necessary to generate an eclogitization increase during deformation. Such diffusion coefficients agree with effective diffusion coefficients and lattice diffusion coefficients for oxygen, H_2O, and light elements measured in laboratory experiments. Our results demonstrate that either numerous repetitive fluid pulses and/or a substantial amount of fluid during strain accumulation was necessary to produce the mapped structures. Finally, we show that shear zone widening during progressive deformation occurs due to a substantial fluid supply and shear zones must be recharged to keep consumption of the wall rock ongoing and build such kilometer-wide shear zones like exposed on Holsnøy.

Data Availability Statement

All data used in this study can be accessed in the supporting information and are accessible via https://osf.io/cvhgf/.

Acknowledgments
The use of the drone during field work was funded by the Norwegian Research Council, project 250327 to T. B. Andersen and we thank Dr. H. J. Kjøll for piloting the drone. This research has been partially supported by the Deutsche Forschungsgemeinschaft (DFG) through grant CRC 1114 "Scaling Cascades in complex Systems," Project Number 235221301, Project (C09)—"Dynamics of rock dehydration on multiple scales." Furthermore, we thank Anja Schleicher and Andrea Gottsche (GFZ Potsdam) for XRF analysis. We also thank Susan Ellis, Philippe Yamato, and one anonymous reviewer for very constructive comments on previous versions of the manuscript. Further editor Margaret E. Rusmore and associate editor Luc Lavier are thanked for editorial handling. Open access funding enabled and organized by Projekt DEAL.

References

Andersen, T. B., Berry, H. N., Lux, D. R., & Andresen, A. (1998). The tectonic significance of pre-Scandian 40Ar/39Ar phengite cooling ages in the Caledonides of western Norway. *Journal of the Geological Society*, *155*(2), 297–309.

Andersen, T. B., Corfu, F., Labrousse, L., & Osmundsen, P.-T. (2012). Evidence for hyperextension along the pre-Caledonian margin of Baltica. *Journal of the Geological Society*, *169*(5), 601–612.

Andersen, T. B., Jamtveit, B., Dewey, J. F., & Swensson, E. J. T. N. (1991). Subduction and eduction of continental crust: Major mechanisms during continent-continent collision and orogenic extensional collapse, a model based on the south Norwegian Caledonides. *Terra Nova*, *3*(3), 303–310.

Austrheim, H. (1987). Eclogitization of lower crustal granulites by fluid migration through shear zones. *Earth and Planetary Science Letters*, *81*(2–3), 221–232.

Austrheim, H. (1998). Influence of fluid and deformation on metamorphism of the deep crust and consequences for the geodynamics of collision zones. In *When continents collide: Geodynamics and geochemistry of ultrahigh-pressure rocks* (pp. 297–323). Dordrecht: Springer.

Austrheim, H., & Boundy, T. M (1994). Pseudotachylytes generated during seismic faulting and eclogitization of the deep crust. *Science*, *265*(5168), 82–83.

Austrheim, H., & Griffin, W. L. (1985). Shear deformation and eclogite formation within granulite-facies anorthosites of the Bergen Arcs, Western Norway, *Chemical Geology*, *50*(1–3), 267–281.

Austrheim, H., & Robins, B. (1981). Reactions involving hydration of orthopyroxene in anorthosite-gabbro. *Lithos*, *14*(4), 275–281.

Bhowany, K., Hand, M., Clark, C., Kelsey, D. E., Reddy, S. M., Pearce, M. A., et al. (2018). Phase equilibria modelling constraints on P–T conditions during fluid catalysed conversion of granulite to eclogite in the Bergen Arcs, Norway. *Journal of Metamorphic Geology*, *36*(3), 315–342.

Boundy, T. M., Fountain, D. M., & Austrheim, H. (1992). Structural development and petrofabrics of eclogite facies shear zones, Bergen Arcs, western Norway: Implications for deep crustal deformational processes. *Journal of Metamorphic Geology*, *10*(2), 127–146.

Boundy, T. M., Mezger, K., & Essene, E. J. (1997). Temporal and tectonic evolution of the granulite-eclogite association from the Bergen Arcs, western Norway. *Lithos*, *39*(3–4), 159–178.

Brady, J. B., & Cherniak, D. J. (2010). Diffusion in minerals: An overview of published experimental diffusion data. *Reviews in Mineralogy and Geochemistry*, *72*(1), 899–920.

Chen, S., Hiraga, T., & Kohlstedt, D. L. (2006). Water weakening of clinopyroxene in the dislocation creep regime. *Journal of Geophysical Research*, *111*, B08203. https://doi.org/10.1029/2005JB003885

Corfu, F., Andersen, T. B., & Gasser, D. (2014). The Scandinavian Caledonides: Main features, conceptual advances and critical questions. *Geological Society, London, Special Publications*, *390*(1), 9–43. https://doi.org/10.1144/sp390.25

Dohmen, R., & Milke, R. (2010). Diffusion in polycrystalline materials: Grain boundaries, mathematical models, and experimental data. *Reviews in Mineralogy and Geochemistry*, *72*(1), 921–970.

Eide, E. A., Torsvik, T. H., Andersen, T. B., & Arnaud, N. O. (1999). Early Carboniferous unroofing in western Norway: A tale of alkali feldspar thermochronology. *The Journal of Geology*, *107*(3), 353–374.

Fossen, H., & Dunlap, W. J. (1998). Timing and kinematics of Caledonian thrusting and extensional collapse, southern Norway: Evidence from $^{40}Ar/^{39}Ar$ thermochronology. *Journal of Structural Geology*, *20*(6), 765–781.

Fossen, H., Geane Carolina, G., & Cavalcante, G. (2017). Shear zones – A review. *Earth-Science Reviews*, *171*, 434–455.

Fountain, D. M., Boundy, T. M., Austrheim, H., & Rey, P. (1994). Eclogite-facies shear zones – Deep crustal reflectors? *Tectonophysics*, *232*(1–4), 411–424.

Fournier, H. W., Lee, J. K. W., & Camacho, A. (2019). Slow cooling versus episodic fluid injections: Deciphering the Caledonian orogeny in Vestvågøy, Lofoten islands, Norway. *Journal of Metamorphic Geology*, *37*(6), 769–793.

Fusseis, F., Handy, M. R., & Schrank, C. (2006). Networking of shear zones at the brittle-to-viscous transition (Cap de Creus, NE Spain). *Journal of Structural Geology*, *28*(7), 1228–1243. https://doi.org/10.1016/j.jsg.2006.03.022

Fusseis, F., Regenauer-Lieb, K., Liu, J., Hough, R., & De Carlo, F. (2009). Creep cavitation can establish a dynamic granular fluid pump in ductile shear zones. *Nature*, *459*(7249), 974–977.

Gee, D. G., & Sturt, B. (1985). *The Caledonide orogen: Scandinavia and related areas*. Wiley.

Gerald, J. F., & Stünitz, H. (1993). Deformation of granitoids at low metamorphic grade. I: Reactions and grain size reduction. *Tectonophysics*, *221*(3–4), 269–297.

Glodny, J., Kühn, A., & Austrheim, H. (2008). Diffusion versus recrystallization processes in Rb-Sr geochronology: Isotopic relics in eclogite facies rocks, Western Gneiss Region, Norway. *Geochimica et Cosmochimica Acta*, *72*(2), 506–525. https://doi.org/10.1016/j.gca.2007.10.021

Hawemann, F., Mancktelow, N. S., Pennacchioni, G., Wex, S., & Camacho, A. (2019). Weak and slow, strong and fast: How shear zones evolve in a dry continental crust (Musgrave Ranges, Central Australia). *Journal of Geophysical Research: Solid Earth*, *124*(1), 219–240. https://doi.org/10.1029/2018JB016559

Hier-Majumder, S. (2005). Water weakening of clinopyroxenite in diffusion creep. *Journal of Geophysical Research*, *110*, B07406. https://doi.org/10.1029/2004jb003414

Incel, S., Labrousse, L., Hilairet, N., John, T., Gasc, J., Shi, F., et al. (2019). Reaction-induced embrittlement of the lower continental crust. *Geology*, *47*(3), 235–238.

Jakob, J., Alsaif, M., Corfu, F., & Andersen, T. B. (2017). Age and origin of thin discontinuous gneiss sheets in the distal domain of the magma-poor hyperextended pre-Caledonian margin of Baltica, southern Norway. *Journal of the Geological Society*, *174*(3), 557–571.

Jakob, J., Andersen, T. B., & Kjøll, H. J. (2019). A review and reinterpretation of the architecture of the South and South-Central Scandinavian Caledonides – A magma-poor to magma-rich transition and the significance of the reactivation of rift inherited structures. *Earth-Science Reviews*, *192*, 513–528.

Jamtveit, B., Austrheim, H., & Malthe-Sørenssen, A. (2000). Accelerated hydration of the Earth's deep crust induced by stress perturbations. *Nature*, *408*, 75–78.

Jamtveit, B., Ben-Zion, Y., Renard, F., & Austrheim, H. (2018a). Earthquake-induced transformation of the lower crust. *Nature*, *556*(7702), 487–491. https://doi.org/10.1038/s41586-018-0045-y

Jamtveit, B., Bucher-Nurminen, K., & Austrheim, H. (1990). Fluid controlled eclogitization of granulites in deep crustal shear zones, Bergen arcs, Western Norway. *Contributions to Mineralogy and Petrology*, *104*(2), 184–193.

Jamtveit, B., Moulas, E., Andersen, T. B., Austrheim, H., Corfu, F., Petley-Ragan, A., & Schmalholz, S. M. (2018b). High pressure metamorphism caused by fluid induced weakening of deep continental crust. *Scientific Reports*, *8*(1), 17011.

Jamtveit, B., Petley-Ragan, A., Incel, S., Dunkel, K. G., Aupart, C., Austrheim, H., et al. (2019). The effects of earthquakes and fluids on the metamorphism of the lower continental crust. *Journal of Geophysical Research: Solid Earth*, *124*(8), 7725–7755. https://doi.org/10.1029/2018JB016461

Jessell, M., & Lister, G. (1991). Strain localization behaviour in experimental shear zones. *Pure and Applied Geophysics*, *137*(4), 421–438.

John, T., & Schenk, V. (2003). Partial eclogitisation of gabbroic rocks in a late Precambrian subduction zone (Zambia): Prograde metamorphism triggered by fluid infiltration. *Contributions to Mineralogy and Petrology*, *146*(2), 174–191. https://doi.org/10.1007/s00410-003-0492-8

Jolivet, L., Raimbourg, H., Labrousse, L., Avigad, D., Leroy, Y., Austrheim, H., & Andersen, T. B. (2005). Softening trigerred by eclogitization, the first step toward exhumation during continental subduction. *Earth and Planetary Science Letters*, *237*(3–4), 532–547. https://doi.org/10.1016/j.epsl.2005.06.047

Karato, S. I. (2008). *Deformation of earth materials. An Introduction to the Rheology of Solid Earth*, 463. http://sutlib2.sut.ac.th/sut_contents/H127485.pdf

Karato, S.-I., & Jung, H. (2003). Effects of pressure on high-temperature dislocation creep in olivine. *Philosophical Magazine*, *83*(3), 401–414.

Kiss, D., Podladchikov, Y., Duretz, T., & Schmalholz, S. M. (2019). Spontaneous generation of ductile shear zones by thermal softening: Localization criterion, 1D to 3D modelling and application to the lithosphere. *Earth and Planetary Science Letters*, *519*, 284–296.

Klemd, R., John, T., Scherer, E. E., Rondenay, S., & Gao, J. (2011). Changes in dip of subducted slabs at depth: Petrological and geochronological evidence from HP–UHP rocks (Tianshan, NW-China). *Earth and Planetary Science Letters*, *310*(1–2), 9–20. https://doi.org/10.1016/j.epsl.2011.07.022

Kühn, A., Glodny, J., Austrheim, H., & Råheim, A. (2002). The Caledonian tectono-metamorphic evolution of the Lindås Nappe: Constraints from U-Pb, Sm-Nd and Rb-Sr ages of granitoid dykes. *Norwegian Journal of Geology*, *82*(1), 45–57.

Labrousse, L., Hetényi, G., Raimbourg, H., Jolivet, L., & Andersen, T. B. (2010). Initiation of crustal-scale thrusts triggered by metamorphic reactions at depth: Insights from a comparison between the Himalayas and Scandinavian Caledonides. *Tectonics*, *29*(5), TC5002. https://doi.org/10.1029/2009tc002602

Lasaga, A. C. (1986). Metamorphic reaction rate laws and development of isograds. *Mineralogical Magazine*, *50*(357), 359–373.

Lasaga, A. C. (1998). *Kinetic theory in the earth sciences*. Princeton University Press.

Mancktelow, N. S. (2008). Tectonic pressure: Theoretical concepts and modelled examples. *Lithos*, *103*(1–2), 149–177.

Marques, F. O., & Burlini, L. (2008). Rigid inclusions rotate in geologic materials as shown by torsion experiments. *Journal of Structural Geology*, *30*(11), 1368–1371.

Menegon, L., Pennacchioni, G., Malaspina, N., Harris, K., & Wood, E. (2017). Earthquakes as precursors of ductile shear zones in the dry and strong lower crust. *Geochemistry, Geophysics, Geosystems*, *18*(12), 4356–4374. https://doi.org/10.1002/2017GC007189

Moulas, E., Burg, J.-P., & Podladchikov, Y. (2014). Stress field associated with elliptical inclusions in a deforming matrix: Mathematical model and implications for tectonic overpressure in the lithosphere. *Tectonophysics*, *631*, 37–49. https://doi.org/10.1016/j.tecto.2014.05.004

Moulas, E., & Schmalholz, S. M. (2020). The importance of interfacial instability for viscous folding in mechanically heterogeneous layers. *Geological Society, London, Special Publications*, *487*(1), 45–58.

Moulas, E., Schmalholz, S. M., Podladchikov, Y., Tajčmanová, L., Kostopoulos, D., & Baumgartner, L. (2019). Relation between mean stress, thermodynamic, and lithostatic pressure. *Journal of Metamorphic Geology*, *37*(1), 1–14. https://doi.org/10.1111/jmg.12446

Nábělek, J., Hetényi, G., Vergne, J., Sapkota, S., Kafle, B., Jiang, M., et al. (2009). Underplating in the Himalaya-Tibet collision zone revealed by the Hi-CLIMB experiment. *Science*, *325*(5946), 1371–1374.

Pennacchioni, G., & Mancktelow, N. (2018). Small-scale ductile shear zones: Neither extending, nor thickening, nor narrowing. *Earth-Science Reviews*, *184*, 1–12.

Petley-Ragan, A., Dunkel, K. G., Austrheim, H., Ildefonse, B., & Jamtveit, B. (2018). Microstructural records of earthquakes in the lower crust and associated fluid-driven metamorphism in plagioclase-rich granulites. *Journal of Geophysical Research: Solid Earth*, *123*(5), 3729–3746. https://doi.org/10.1029/2017JB015348

Plümper, O., Botan, A., Los, C., Liu, Y., Malthe-Sørenssen, A., & Jamtveit, B. (2017). Fluid-driven metamorphism of the continental crust governed by nanoscale fluid flow. *Nature Geoscience*, *10*(9), 685–690.

Pollard, D., & Fletcher, R. C. (2005). *Fundamentals of structural geology*. Cambridge University Press. Retrieved from http://repository.fue.edu.eg/xmlui/bitstream/handle/123456789/2767/7722.pdf?sequence=1&isAllowed=y

Putnis, A., Jamtveit, B., & Austrheim, H. (2017). Metamorphic processes and seismicity: The Bergen Arcs as a natural laboratory. *Journal of Petrology*, *58*(10), 1871–1898. https://doi.org/10.1093/petrology/egx076

Putnis, A., & John, T. J. E. (2010). Replacement processes in the Earth's crust. *Elements*, *6*(3), 159–164.

Raimbourg, H., Jolivet, L., Labrousse, L., Leroy, Y., & Avigad, D. (2005). Kinematics of syneclogite deformation in the Bergen Arcs, Norway: Implications for exhumation mechanisms. *Geological Society, London, Special Publications*, *243*(1), 175–192. https://doi.org/10.1144/gsl.Sp.2005.243.01.13

Raimbourg, H., Jolivet, L., & Leroy, Y. (2007). Consequences of progressive eclogitization on crustal exhumation, a mechanical study. *Geophysical Journal International*, *168*(1), 379–401. https://doi.org/10.1111/j.1365-246X.2006.03130.x

Ramsay, J., & Huber, M. I. (1983). *The techniques of modern structural geology. Vol. 1, Strain analysis*. Academic Press.

Räss, L., Duretz, T., Podladchikov, Y. Y., & Schmalholz, S. M. (2017). M2Di: Concise and efficient MATLAB 2-D Stokes solvers using the Finite Difference Method. *Geochemistry, Geophysics, Geosystems*, *18*(2), 755–768. https://doi.org/10.1002/2016GC006727

Roberts, D. (2003). The Scandinavian Caledonides: Event chronology, palaeogeographic settings and likely modern analogues. *Tectonophysics*, *365*(1–4), 283–299.

Rondenay, S., Abers, G. A., & van Keken, P. E. (2008). Seismic imaging of subduction zone metamorphism. *Geology*, *36*(4), 275–278. https://doi.org/10.1130/g24112a.1

Schmid, R., Altenberger, U., & Oberhänsli, R. (1998). *Polyphase tectono-metamorphic evolution of the northwestern Lindas Nappe on Holsnoy, Bergen Arcs, Caledonides, SW-Norway*. Zentralblatt für Geologie und Palaeontologie / Teil.

Schneider, F., Yuan, X., Schurr, B., Mechie, J., Sippl, C., Haberland, C., et al. (2013). Seismic imaging of subducting continental lower crust beneath the Pamir. *Earth and Planetary Science Letters*, *375*, 101–112.

Taetz, S., John, T., Bröcker, M., Spandler, C., & Stracke, A. (2018). Fast intraslab fluid-flow events linked to pulses of high pore fluid pressure at the subducted plate interface. *Earth and Planetary Science Letters*, *482*, 33–43.

Terry, M. P., & Heidelbach, F. (2006). Deformation-enhanced metamorphic reactions and the rheology of high-pressure shear zones, Western Gneiss Region, Norway. *Journal of Metamorphic Geology*, *24*(1), 3–18. https://doi.org/10.1111/j.1525-1314.2005.00618.x

Yuan, X., Sobolev, S. V., Kind, R., Oncken, O., Bock, G., Asch, G., et al. (2000). Subduction and collision processes in the Central Andes constrained by converted seismic phases. *Nature*, *408*, 958–961.

Zertani, S., John, T., Tilmann, F., Motra, H. B., Keppler, R., Andersen, T. B., & Labrousse, L. (2019a). Modification of the seismic properties of subducting continental crust by eclogitization and deformation processes. *Journal of Geophysical Research: Solid Earth*, *124*(9), 9731–9754.

Zertani, S., Labrousse, L., John, T., Andersen, T. B., & Tilmann, F. (2019b). The interplay of eclogitization and deformation during deep burial of the lower continental crust – A case study from the Bergen Arcs (Western Norway). *Tectonics*, *38*, 898–915. https://doi.org/10.1029/2018TC005297